



Interstitial Nature of Mn 2+ Doping in 2D Perovskites

Andrew Torma, Wenbin Li, Hao Zhang, Qing Tu, Vladislav Klepov, Michael Brennan, Christopher Mccleese, Matthew Krzyaniak, Michael Wasielewski, Claudine Katan, et al.

► To cite this version:

Andrew Torma, Wenbin Li, Hao Zhang, Qing Tu, Vladislav Klepov, et al.. Interstitial Nature of Mn 2+ Doping in 2D Perovskites. ACS Nano, 2021, 15 (12), pp.20550-20561. 10.1021/acsnano.1c09142 . hal-03481423

HAL Id: hal-03481423

<https://hal.science/hal-03481423>

Submitted on 22 Feb 2022

HAL is a multi-disciplinary open access archive for the deposit and dissemination of scientific research documents, whether they are published or not. The documents may come from teaching and research institutions in France or abroad, or from public or private research centers.

L'archive ouverte pluridisciplinaire **HAL**, est destinée au dépôt et à la diffusion de documents scientifiques de niveau recherche, publiés ou non, émanant des établissements d'enseignement et de recherche français ou étrangers, des laboratoires publics ou privés.



Distributed under a Creative Commons Attribution - NonCommercial 4.0 International License

Interstitial Nature of Mn²⁺ Doping in 2D Perovskites

Andrew J. Torma^{1,2#}, Wenbin Li^{1,2#}, Hao Zhang^{1,2}, Qing Tu³, Vladislav V. Klepov⁴, Michael C. Brennan⁵, Christopher L. McCleese^{5,6}, Matthew D. Krzyaniak⁷, Michael R. Wasielewski⁷, Claudine Katan⁸, Jacky Even⁹, Martin V. Holt¹⁰, Tod A. Grusenmeyer⁵, Jie Jiang⁵, Ruth Pachter⁵, Mercouri G. Kanatzidis⁴, Jean-Christophe Blancon^{1*}, and Aditya D. Mohite^{1,2*}

¹Department of Chemical and Biomolecular Engineering, Rice University, Houston, TX 77005, USA

²Applied Physics Program, Smalley-Curl Institute, Rice University, Houston, TX 77005, USA

³Department of Materials Science and Engineering, Texas A&M University, College Station, TX 77843, USA

⁴Department of Chemistry and Department of Materials Science and Engineering, Northwestern University, Evanston, IL 60208, USA

⁵Air Force Research Laboratory, Materials and Manufacturing Directorate, Wright-Patterson Air Force Base, Dayton, Ohio 45433, USA

⁶General Dynamics Information Technology, 5000 Springfield Pike, Dayton, Ohio 45431, USA

⁷Department of Chemistry and Institute for Sustainability and Energy at Northwestern, Northwestern University, Evanston, IL 60208-3113, USA

⁸Univ Rennes, ENSCR, INSA Rennes, CNRS, ISCR (Institut des Sciences Chimiques de Rennes)–UMR 6226, F-35000 Rennes, France

⁹Univ Rennes, INSA Rennes, CNRS, Institut FOTON–UMR 6082, F-35000 Rennes, France

¹⁰Center for Nanoscale Materials, Argonne National Laboratory, Lemont, IL 60439, USA

[#]These authors contributed equally

*Correspondence to: blanconjc@gmail.com, adm4@rice.edu

Abstract:

Halide perovskites doped with magnetic impurities (such as the transition metals Mn^{2+} , Co^{2+} , Ni^{2+}) are being explored for a wide range of applications beyond photovoltaics, such as spintronic devices, stable light-emitting diodes, single-photon emitters, and magneto-optical devices. However, despite several recent studies, there is no consensus on whether the doped magnetic ions will predominantly replace the octahedral B-site metal *via* substitution or reside at interstitial defect sites. Here, by performing correlated nanoscale X-ray microscopy, spatially and temporally resolved photoluminescence measurements, and magnetic force microscopy on the inorganic 2D perovskite $\text{Cs}_2\text{PbI}_2\text{Cl}_2$, we show that doping Mn^{2+} into the structure results in a lattice expansion. The observed lattice expansion contrasts with the predicted contraction expected to arise from the B-site metal substitution, thus implying that Mn^{2+} does not replace the Pb^{2+} sites. Photoluminescence and electron paramagnetic resonance measurements confirm the presence of Mn^{2+} in the lattice, while correlated nano-XRD and X-ray fluorescence track the local strain and chemical composition. Density functional theory calculations predict that Mn^{2+} atoms reside at the interstitial sites between two octahedra in the triangle formed by one Cl^- and two I^- atoms, which results in a locally expanded structure. These measurements show the fate of the transition metal dopants, the local structure, and optical emission when they are doped at dilute concentrations into a wide band-gap semiconductor.

Keywords: halide perovskites, crystal structure, transition metals, doping, density functional theory, strain mapping, nano X-ray diffraction

The use of wide band-gap semiconductors as hosts for metal doping has been widely explored over the past couple of decades to create dilute magnetic semiconductors that can potentially demonstrate ferromagnetic behavior at ambient conditions. While there have been a wide range of semiconductor material systems that have been used as hosts, the choices for the magnetic dopants have been mainly transition metals, such as first row metals (Mn^{2+} , Co^{2+} , Ni^{2+} , Cu^{2+}) and lanthanides (Eu^{2+} , Er^{3+} , Sm^{3+} , Yb^{3+}).^{1,2} Out of these, there has been extensive work on the incorporation and effects of Mn^{2+} .^{3,4} This includes structural and chemical changes, dopant destination (spatially), and energy transfer dynamics of host to Mn^{2+} that results in a signature 580-600 nm emission. Prominent host materials have been $\text{Zn}(\text{S,Se,O})$ ^{1,5,6,7,8,9,10} or $\text{Cd}(\text{S,Se})$ ^{9,11,12,13}

nanocrystals and quantum dots, or III-V semiconductor films and nanowires.^{14,15,16,17,18} Notable performance improvements in optoelectronic applications of these semiconductors in solar cells¹⁹ and hot electrons for photocatalysis²⁰ have been reported. However, more intriguing has been the observation of magneto-optical and magneto-transport properties^{21,22,23,24} which includes high temperature ferromagnetic semiconductors (up to 425 K for doping < 4 at %),^{25,26,27} spin injection,²⁸ and spin polarized emission^{29,30,31} for potential spintronics. Interestingly, the mechanism of incorporating Mn^{2+} atoms either through substitution of a host metal or at interstitial sites has shown to significantly impact these magnetic properties, such as dopant clustering nullifying the magnetic moment or interstitials disrupting ferromagnetic ordering and carry densities,^{15,25} where different synthesis strategies have demonstrated effects on dopant incorporation. For example, lower temperature growth or decrease in film thickness resulting in less dopant clustering,^{21,25} chemical vapor deposition promoting substitution,²⁷ and post-growth annealing aiding out-diffusion of interstitials in thin films.¹⁵ Furthermore, semiconductor hosts are continually being investigated to overcome the limited host emission tunability, impurity tolerance, and taxing synthesis processes of the previously described materials.³²

Inspired by their exceptional optoelectronic properties, chemical and structural tunability, and solution processed synthesis^{32,33,34,35,36,37,38} both 3D (ABX_3 , where A = organic or inorganic cation, B = divalent metal cation, X = I, Cl, Br) and 2D ($\text{A}_2'\text{A}_{n-1}\text{B}_n\text{X}_{3n+1}$, where A' = spacer cation, such as Cs^+ and MA^+) halide perovskites (HaPs) are being used as hosts for doping with ferromagnetic divalent metal ions with the goal of exploring applications in spintronics, non-linear optics, and quantum information.³⁹ Incorporation of the transition metals into HaPs can occur *via* two pathways: by substitution with the B-site divalent metal or by occupation of interstitial sites in the lattice. Depending on the incorporation type, the dopant would affect the system differently, leading to distinct changes in the lattice and band structures creating measurable structural and optical signatures.

A popular magnetic metal dopant of choice has been Mn^{2+} , which has been widely used to dope HaPs. While initial challenges existed in incorporating Mn^{2+} into the lattice, recent work has shown efficient doping of Mn^{2+} in high ratios through increasing temperature synthesis,⁴⁰ where an improvement in the stability of certain HaP hosts has also been observed. The enhanced stability is thought to arise from the formation of a much stronger Mn-Cl bond.⁴¹ Once doped, it exhibits a characteristic emission at 2.066 eV (600 nm) attributed to the transition in mid-gap states formed

by the Mn^{2+} d-orbitals (${}^4\text{T}_1 - {}^6\text{A}_1$) through an efficient energy transfer from the ground state exciton in HaPs, where the fundamental band-gap remains unaltered.^{42,43,44,45,46,47,48} The emission from Mn^{2+} is also associated with a photoluminescence lifetime of micro- to milliseconds attributed to the spin forbidden nature of the transition.^{42,49,50} Recent reports have additionally shown that the emission energy is tunable dependent on synthesis and precursor ratios.^{51,40,52} For example, Sun *et al.* demonstrated orange-red emission in 25% $\text{Mn}:\text{PEA}_2\text{PbBr}_4$ (PEA = phenethylamine) through increasing local crystal field strength by incorporating additional amounts of the PEA cation.⁵³ Further, similar to III-V and row IV-semiconductors, Mn^{2+} doping has shown to produce ferromagnetic properties in nonmagnetic perovskite hosts.^{54,55,56} The observations of these optical and magnetic phenomena have been useful in validating the presence of Mn^{2+} dopant in samples and for magneto-optical applications. However, there is a lack in understanding the dopant incorporation type in these systems.

Recent literature has delved into studying the structural phenomena that occur when metal dopants are introduced into the lattice of both all-inorganic and hybrid HaPs. However, there are conflicting reports on the observed structural changes across HaP micro- and nanocrystal structures. Based on Goldsmith's tolerance factor, Mn^{2+} is expected to replace the B-site divalent metal at the center of the metal-halide octahedra similar to other dilute magnetic semiconductors, such as Mn^{2+} substituting divalent Zn^{2+} in the center of the metal-oxide tetrahedra in ZnO .²⁵ Given the smaller size of Mn^{2+} (ionic radius of 0.97 Å) compared to the B-site metal, such as Pb^{2+} (1.33 Å),⁵⁷ a contraction in the lattice is expected and has been reported through XRD measurements in many inorganic structures with >1% nominal doping.^{42,43,52} For example, Acharya *et al.* showed a minor contraction through powder XRD in 2-5% Mn^{2+} doped $\text{Cs}_2\text{PbI}_2\text{Cl}_2$ nanocrystals.⁵⁸ On the other hand, in these low doping amounts, Dutta *et al.* measured no change^{44,45,54} in the d-spacing for 1.7% Mn^{2+} doping in $\text{Cs}_2\text{PbI}_2\text{Cl}_2$ nanoplatelets,⁵⁹ and in contrast, Das Adhikari *et al.* showed an expansion in the lattice for 2% Mn^{2+} doping in CsPbCl_3 nanocrystals.⁶⁰ Comparatively, a variety of Mn^{2+} doped hybrid HaPs micro- and nanocrystal structures have also reported the expected lattice contraction for substitutional incorporation.^{53,61,62,63,64,65} Again, in these doped hybrid HaPs systems similar to the inorganic systems, there are further reports of no change in the lattice.^{47,51}

In either inorganic or hybrid HaPs, the connection to the host lattice or dopant density of Mn^{2+} and structural changes remain unclear, where characterization has been limited to macroscopic observations through conventional XRD techniques. Similar reports on macroscopic

structures, such as thin films, have also shown both contraction and expansion,^{66,67} but propose an explanation based on dopant incorporation mode. For example, Sun *et al.* observed expansions in the lattice of MAPbI₃ films with an increased amount of Mn²⁺ dopant attributed to the soft lattice nature of the film that allowed for the Mn²⁺ ions to be located in a variety of interstitial positions creating charges at grain boundaries.⁶⁸ In contrast, interstitial positions would exist in much smaller volume in the micro- and nanostructures explored above. We may hypothesize that expansions in the lattice occur as the Mn²⁺ dopant resides at interstitial sites initially, where the overall contraction from the expected substitution dominates at higher doping amounts. The majority of studies that report no change in d-spacing is at these lower doping regimes and result from the incorporated dopant fraction being too small to be picked up by bulk measurements. Local probing is needed, thus motivating our study.

Here, we performed comprehensive structural characterization to understand Mn²⁺ doping into the all-inorganic Ruddlesden-Popper 2D HaP, Cs₂PbI₂Cl₂. With the goal of understanding discretized dopant-host interactions and local structure, we focus on incorporation of dilute doping concentration 0.1% Mn²⁺. By leveraging the advanced confocal X-ray microscopy technique, along with optical and magnetic methods such as magnetic force microscopy and electron paramagnetic resonance, we track the local nanoscale strain and chemical concentration of the 2D inorganic perovskite. Contrary to previous reports^{58,59} and as anticipated from the Goldschmidt's tolerance factor, we observe an overall lattice expansion across different Mn²⁺ dopant concentrations. DFT simulations predicts lattice expansion arises from Mn²⁺ dopants occupying interstitial sites in the voids between the octahedral Cl and I, thus supporting our experimental findings. These fundamental results show the fate of magnetic divalent metal ions doped into the host perovskite lattice and may be potentially relevant for the design of single photon emitters for a wide range of applications.

Results & Discussion

The inorganic 2D HaP Cs₂PbI₂Cl₂ single crystals were synthesized using a standard melt growth process. Briefly, stoichiometric amounts of CsI and PbCl₂ were sealed in a silica tube (Figure S1) and heated to 500°C above the melting point of the precursors then allowed to slowly cool to form crystals with the targeted stoichiometry.⁶⁹ To achieve the nominal doping amount of 0.1-10% Mn²⁺, the respective molar amount of PbCl₂ was substituted by MnCl₂ in the reaction.

The pristine 2D perovskite lattice consists of a single layer ($n = 1$) of the $\text{PbI}_2\text{Cl}_2^{2-}$ octahedra with Cs^+ cations acting as the spacer between the octahedra, thereby creating a layered material as illustrated in Figure 1a.⁶⁹ This schematic shows the tetragonal (lattice parameters $a=b \neq c$) Ruddlesden-Popper phase, where the octahedra and spacer cation layers are offset by half a unit cell. The out-of-plane peak (00l) is denoted by the horizontal yellow line in Figure 1a, whose planes are perpendicular to the stacking axis (c-axis); whereas the in-plane peak (hk0) has planes perpendicular to the a and b-axis. Because of this, the (00l) reflections relay information on the layer stacking of the material, while the (hk0) reflections give details on the layers themselves. Figure 1b compares the powder XRD patterns of the 2D perovskites doped with nominal 0-10% Mn^{2+} with the simulated diffraction pattern for the known tetragonal Ruddlesden-Popper crystal structure of $\text{Cs}_2\text{PbI}_2\text{Cl}_2$. Here, the three out-of-plane peaks (002), (004), and (006), along with the in-plane peak (110), are denoted. The diffraction pattern matches with the simulated pattern for

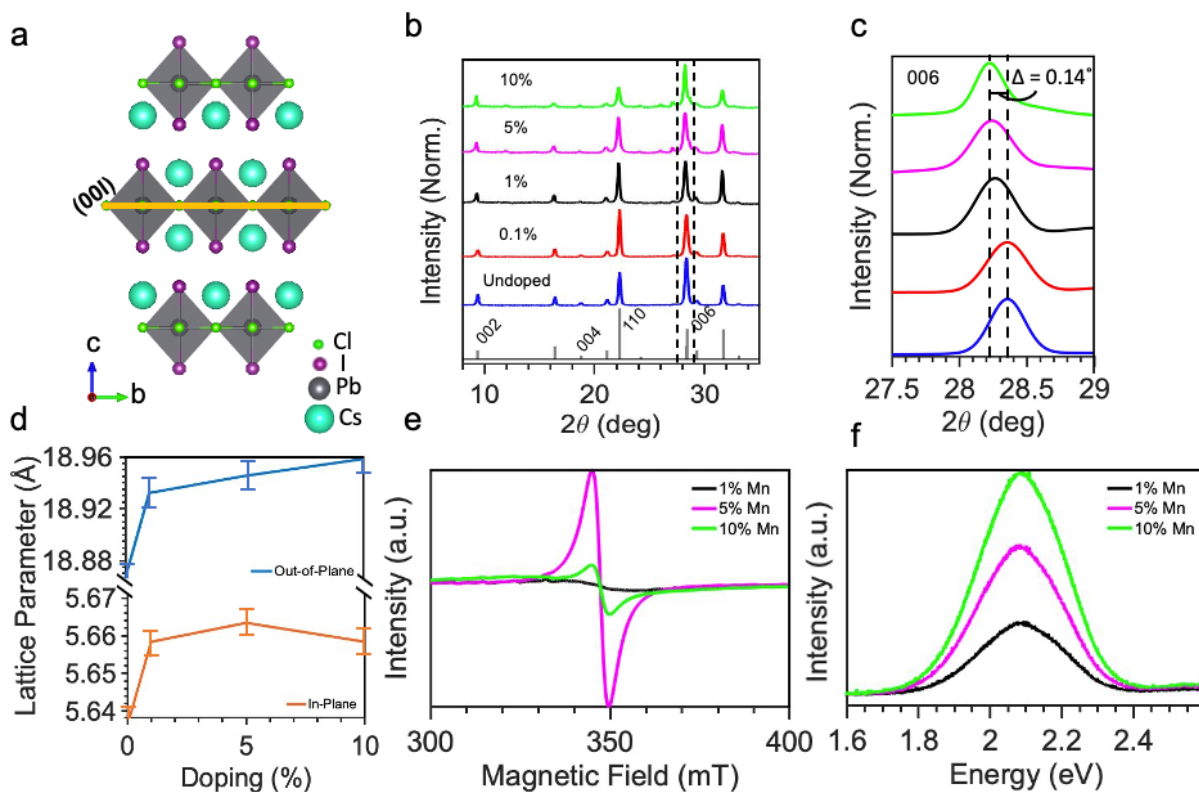


Figure 1. Bulk Structural Characterization. (a) crystal structure of $\text{Cs}_2\text{PbI}_2\text{Cl}_2$ (Colors denote Pb-black, Cs-mint green, I-purple, Cl-green) (b) PXRD spectra for 0-10% Mn^{2+} nominal doping (c) Rietveld refinement of the (006) peak for 0-10% Mn^{2+} nominal doping ($\pm 0.01^\circ$) (d) in-plane ($\pm 0.003 \text{\AA}$) vs out-of-plane ($\pm 0.007 \text{\AA}$) lattice parameter changes as a function of Mn doping (e) EPR signal and (f) PL of Mn^{2+} signal for 1-10% Mn^{2+} nominal doping.

the intrinsic reference crystal, thus validating tetragonal Ruddlesden-Popper phase of $\text{Cs}_2\text{PbI}_2\text{Cl}_2$. Closer examination of the in-plane and the out-of-plane peaks were conducted using Rietveld refinements, which revealed a slight shift to lower diffraction angles with increasing Mn^{2+} doping concentration. Specifically, the (110) peak showed a maximum change of $0.009 \pm 0.001 \text{ \AA}^{-1}$ ($\Delta 2\theta = 0.12^\circ \pm 0.01^\circ$) (Table S1), and the (006) peak a maximum change of $0.010 \pm 0.001 \text{ \AA}^{-1}$ ($\Delta 2\theta = 0.14^\circ \pm 0.01^\circ$) with increasing Mn^{2+} doping as shown in Figure 1c. The 0.1% Mn system did not show a shift in the diffraction peaks, but we observe a slight broadening of $0.003 \pm 0.001 \text{ \AA}^{-1}$ ($\Delta 2\theta = 0.04^\circ \pm 0.01^\circ$) in the full-width-half-maximum (FWHM) of the out-of-plane (006) peak (Table S1). We hypothesize the increase in the FWHM derives from the inhomogeneous incorporation of the dilute amount of Mn^{2+} dopant. For samples doped with higher concentrations of Mn^{2+} , a lattice parameter expansion is observed in both the out-of-plane and in-plane directions of up to 0.48% and 0.53%, respectively (Figure 1d). Interestingly, both parameters have an initial increase up to 1% Mn^{2+} doping that then remains generally constant within error for increased doping of 1-10% Mn^{2+} , indicating the effect saturates. Based on the Goldschmidt's tolerance factor, the substitutional replacement of Pb^{2+} with Mn^{2+} is expected to result in an overall contraction in the lattice (smaller Mn^{2+} replacing the larger Pb^{2+}).^{59,63} In contrast, we observe an overall expansion of the lattice upon Mn^{2+} doping for all concentrations. This expansion suggests that the Mn^{2+} dopant must reside at interstitial sites within the crystal lattice.

To confirm the presence of the Mn^{2+} atoms in these samples, electron paramagnetic resonance (EPR) and photoluminescence (PL) spectroscopy were conducted due to the paramagnetic nature of Mn^{2+} and the distinct yellowish-orange emission (Figure 1e,f). We note an EPR signal was retrieved around 350 mT for 1-10% Mn doping concentration, and a correlated PL emission at 2.09 eV (594 nm) was observed for the same samples independent of the doping concentrations. Interestingly, the EPR signal decreases from the 5% to 10% Mn^{2+} concentration, conversely, the PL emission grows in intensity with increased doping amount. Because of this, the drop cannot be attributed to a lowering amount of Mn^{2+} in the sample. Instead, single Mn^{2+} atoms are paramagnetic in nature, but induced coupling is known to occur between Mn^{2+} atoms in close approximation to each other producing antiferromagnetic clusters.⁵⁵ Therefore, a decrease in EPR signal was observed with clustering as once measurable unpaired electrons couple together with electrons of opposite spin in surrounding Mn^{2+} atoms.⁵⁴ This confirmed the presence of Mn^{2+} atoms in the 1-10% Mn: $\text{Cs}_2\text{PbI}_2\text{Cl}_2$ samples with tendencies to cluster at higher doping amounts.

Moreover, PL spectroscopy performed on the series of samples for 1%, 5%, and 10% Mn^{2+} doping remains invariant. Therefore, in order to truly understand local doping on the structural properties and disentangle the effects of conglomeration and Mn-Mn interactions with the ultimate goal of creating single photon emission sites, we focused on the $\text{Mn}:\text{Cs}_2\text{PbI}_2\text{Cl}_2$ system with 0.1% doping as described in the remainder of the manuscript. The existence of Mn^{2+} and spatial characteristics were investigated using steady-state and time-resolved PL and magnetic force microscopy (MFM), while local structural changes (resolution of 20 nm) were investigated through correlated nanoscale confocal XRD (nanoXRD) and X-ray fluorescence (nanoXRF) imaging.

Figure 2a shows the absorbance spectra (black) and the corresponding photoluminescence spectra (red) of each sample obtained by making a crushed powder on a quartz substrate (see details in Methods). The absorption and PL spectra for the undoped sample are in good agreement with previous measurements on $\text{Cs}_2\text{PbI}_2\text{Cl}_2$, exhibiting an onset of absorbance and PL emission at 2.88 eV (430 nm).⁶⁹ For the doped sample, while the absorbance spectra is almost identical to the undoped sample, the photoluminescence spectra showed another distinct peak at 2.06 eV (602 nm), which was not present in the PL spectra of the undoped sample. The peak position is slightly lower in energy, red shifted by 0.03 eV, from the PL signal measured on the higher doped samples. Nevertheless, this is in good agreement with previous results of a Mn^{2+} induced PL signal around 2.07 eV (599 nm)^{59,60,64} and confirms the presence of Mn^{2+} in the 2D perovskite. To gain a deeper insight into the optical properties, we performed time-resolved PL measurements on the 2.06 eV (602nm) emission peak to characterize the PL decay kinetics (Figure 2b), where the PL kinetics of the intrinsic PL emission (2.88 eV) were previously measured and detailed by our collaborators which showed an average decay lifetime of 3.7 ns.⁶⁹ A monoexponential decay fit was made to the signal peak (black curve) up to 2 ms, as shown by the red line, where the fit parameters can be seen in the *Supporting Information*. Compared to the nanosecond PL lifetime of the intrinsic emission, the fit reveals a PL lifetime of 480 μs , whose long lifetime is indicative of the spin forbidden Mn^{2+} d-shell transition $^4\text{T}_1 - ^6\text{A}_1$.⁴² The observation of a 2.06 eV emission aligns with our measurements on higher dopes samples, and the long PL lifetime on the scale of microseconds is in agreement with current literature on Mn-doped 2D HaPs.^{47,59} Therefore, the PL data confirms the incorporation of Mn^{2+} into our 0.1% $\text{Mn}:\text{CsPbI}_2\text{Cl}_2$ sample.

Due to the magnetic nature of Mn^{2+} atoms, spatial characterization of the dopant was investigated with the aim of finding magnetic signatures using magnetic force microscopy (MFM) across a 2D region on single crystal samples. The $\text{Mn}:\text{CsPbI}_2\text{Cl}_2$ sample exhibits drastically different MFM images compared to undoped $\text{CsPbI}_2\text{Cl}_2$ (Figure 2c,d). As shown in Figure 2d, small attractive magnetic domains with diameters around 30 nm can be found on the 0.1% $\text{Mn}:\text{Cs}_2\text{PbI}_2\text{Cl}_2$ sample with very high contrast, which are denoted by red-dotted circles. As described in the Methods section, the atomic force microscopy (AFM) tip is lifted off from the sample surface, leading to a broadening effect on the feature sizes thus implying that the true sizes of these magnetic features are even smaller. We note that many features manifesting strong repulsive forces (bright regions in Figure 2c) due to strong short-range tip-sample interactions in tapping mode phase images do not show up in the MFM phase images (Figure 2d). Unlike the tapping mode where the phase shift caused by short-range tip-sample interactions and magnetic forces are convoluted, the MFM phase image provides much higher contrast for the magnetic domains. Interestingly, the domains found in MFM phase images are smaller than and different

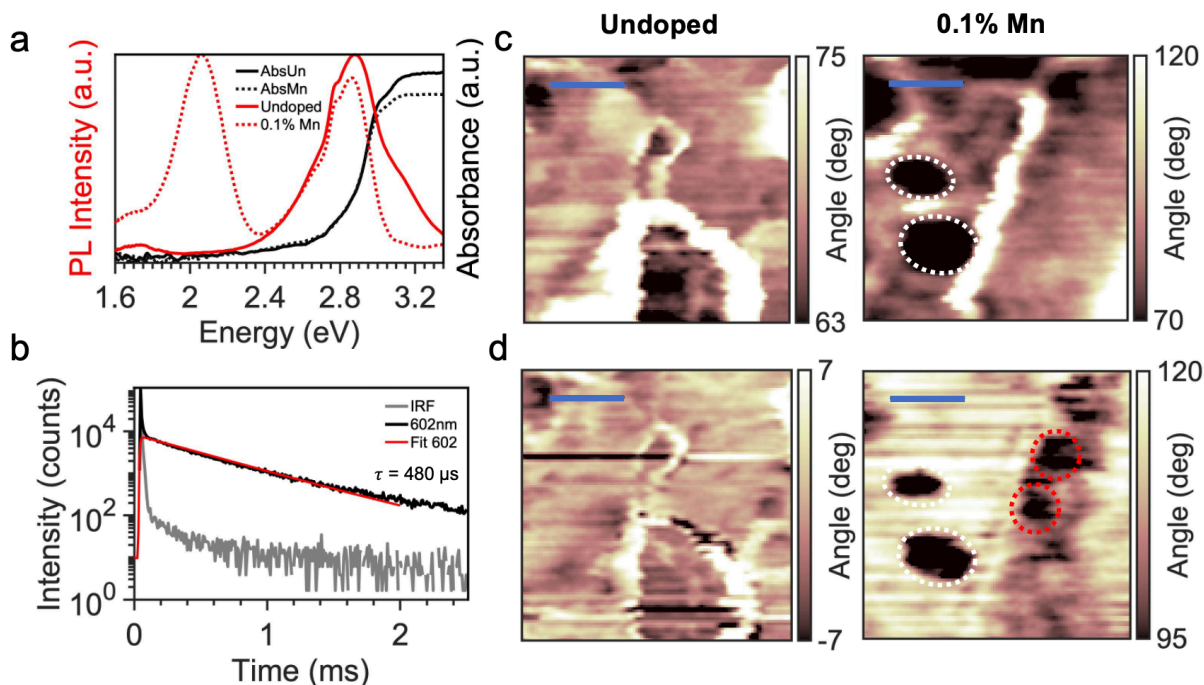


Figure 2. Optical and magnetic characterization. Above band-gap excitation (a) PL and absorbance spectra (b) time-resolved PL of the 0.1% Mn^{2+} sample at 602 nm (2.06 eV) with mono-exponential fitting, where IRF is the instrument response function. MFM (c) tapping mode of undoped (left) and 0.1% Mn^{2+} (right) $\text{Cs}_2\text{PbI}_2\text{Cl}_2$ (d) magnetic phase mode of undoped (left) and 0.1% Mn^{2+} (right) $\text{Cs}_2\text{PbI}_2\text{Cl}_2$. Scalebar is 60 nm. White-dotted circles denote tapping mode features, while the red-dotted circles denote magnetic phase only features.

from the corresponding features on the topographic phase (Figure 2c) and height images (Figure S2). This allows us to identify artifacts arising from topographic crosstalk, as denoted by white dotted circles. In contrast, the undoped sample does not show any of the high contrast, attractive magnetic domains in the MFM phase image (Figure 2d). The features on the MFM phase image largely resemble those found in both topographic phase (Figure 2c) and height images (Figure S2) in terms of their shapes and sizes. Moreover, the contrast of these features compared to the background on MFM phase images (Figure 2d) is even lower than that found in the corresponding topographic phase images (Figure 2c) thus indicating that all the features in the MFM phase image of undoped samples can be identified as non-magnetic artifacts. These measurements reveal the inhomogeneity in the spatial incorporation of Mn^{2+} atoms and suggests clustering of the Mn^{2+} dopant.

To explore how the Mn^{2+} dopant incorporation affects the local crystal structure of $\text{Cs}_2\text{PbI}_2\text{Cl}_2$, nanoscale strain in micrometer-sized cleaved single crystals were investigated through changes in the d-spacing. The magnitude and the mapping of these localized lattice changes in the structure of the perovskite was obtained through nanoscale scanning X-ray microscopy (Figure 3a). This technique measures the correlated nanoXRD and nanoXRF signatures while scanning across the same area of the crystal. Because of the high energy and small beam size of the nanoprobe, the system can penetrate into the bulk of the material and map a 2D region down to 20 nm x 20 nm in resolution. The stability of the crystal under the radiation of the synchrotron source was confirmed through a time series measurement due to the hard-probe nature of the system (Figure 3b). The nanoXRD returns a CCD camera diffraction map (Figure S3), whereby integrating along constant theta lines can be used to interpret the d-spacing at each 20x20 nm spot. In addition, we also measured the nanoXRF, which measured the element dependent integrated fluorescence intensity at each spot (Figure 3d). The diffraction detector was set up to perform high-resolution profiles of the out-of-plane (006) peak. This higher order peak was chosen because of the 2θ range limitation of the apparatus and the pronounced signal in the bulk single crystal XRD. A theta tilt series was conducted to find the best Bragg condition through finding the max diffraction intensity by slight variations in the incident angle (θ_i) (Figure 3c). The undoped $\text{Cs}_2\text{PbI}_2\text{Cl}_2$ sample showed a Bragg peak at $\theta_i = 13.8^\circ$, and while $\text{Mn}:\text{Cs}_2\text{PbI}_2\text{Cl}_2$ also showed a peak at $\theta_i = 13.8^\circ$, an equally strong peak at $\theta_i = 13.6^\circ$ further emerged as illustrated in Figure 3c. The diffraction maxima at $\theta_i = 13.6^\circ$ indicates that an additional Bragg condition arises in the Mn-

doped sample. An average diffraction spectrum across a $1\ \mu\text{m} \times 1\ \mu\text{m}$ region of both the $\text{Cs}_2\text{PbI}_2\text{Cl}_2$ and $\text{Mn}:\text{Cs}_2\text{PbI}_2\text{Cl}_2$ crystals are plotted at the undoped Bragg condition ($\theta_i = 13.8^\circ$) (Figure 3e). In agreement with our bulk powder and single crystal XRD, a distinct widening of the doped sample peak was observed. When performing the same analysis at the second Bragg condition ($\theta_i = 13.6^\circ$), the doped sample showed a low angle shoulder implying an expansion in the out-of-plane direction (Figure 3f). The structural diffraction peak for the undoped sample was at $7.51\ \text{\AA}^{-1}$ ($2\theta = 27.32^\circ$), while the additional feature in the doped 2D perovskite was at a lower d-spacing of $6.99\ \text{\AA}^{-1}$ ($2\theta = 27.08^\circ$) consistent with the observations from bulk single crystal XRD.

With the correct Bragg conditions derived, the 2D single crystal physical boundaries were mapped out using the XRF signal from iodine since it exhibited the strongest intensity (Figure 3d). A $1\ \mu\text{m} \times 1\ \mu\text{m}$ regions of both undoped and doped crystals were chosen for mapping of structural characteristics and are denoted by the blue dotted rectangles in Figure 3d. The centroidal 2θ was derived from the integrated nanoXRD intensity at each step and was used to calculate the d-spacing through Bragg's law. For the undoped system, there was a gradual d-spacing change over the

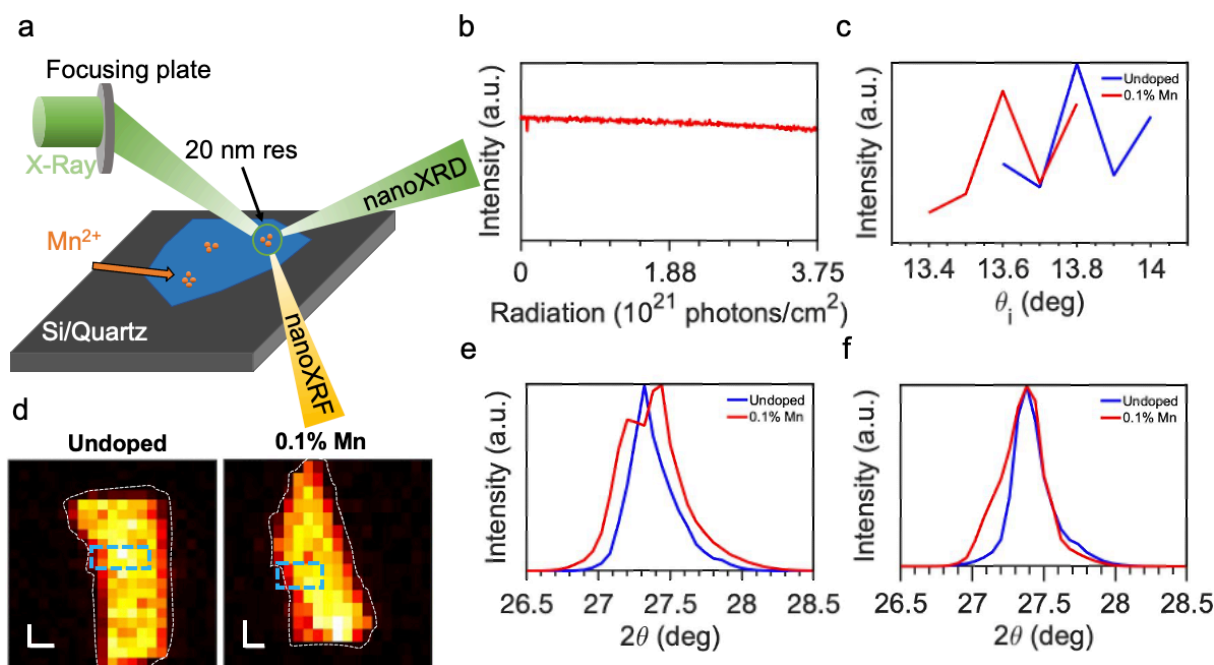


Figure 3. Nanoprobe scanning X-Ray Diffraction and Fluorescence Microscopy. (a) Schematic (b) stability under the X-ray beam radiation (c) diffraction intensity dependent on incident angle (θ_i) (d) undoped (left) vs 0.1% Mn^{2+} (right) full crystal iodine nanoXRF. y-scale bar is $1\ \mu\text{m}$ and x-scale bar is $0.5\ \mu\text{m}$. (e) average diffraction spectrum of a $1\ \mu\text{m} \times 1\ \mu\text{m}$ region at $\theta_i = 13.8^\circ$ (f) average diffraction spectrum of a $1\ \mu\text{m} \times 1\ \mu\text{m}$ region at $\theta_i = 13.6^\circ$.

region from left to right as seen in the change from cool to warm colors (Figure 4a). The left side of the region mapped sits along the edge of the crystal, as seen in the Figure 3d. Hence, this can be attributed to edge effects, which can cause spatially large and gradual strain in the sample. Here, this smooth effect specifically relates to a lattice contraction induced at the edge. The right side relates to the bulk region (shown in Figure 3d) and indeed showed a d-spacing value of 3.15 Å ($2\theta = 27.32^\circ$), which agrees with the average diffraction spectrum from Figure 3e,f. The Mn-doped crystals showed a similar gradual lattice strain at the scale of the sample going away from the edge of the crystal (left to right) (Figure 4a). The Mn-doped system showed the same d-spacing value of 3.15 Å as the undoped intrinsic structure in the bulk region. However, there are also interspersed regions of deep red spots of 50-100 nm in size. These spots exhibit a higher d-spacing value of 3.17 Å ($2\theta = 27.08^\circ$), which relates to a 0.63% expansive strain in the structure. These locally strained regions coincide with the shoulder observed in the average nanoXRD spectrum of the Mn:Cs₂PbI₂Cl₂ system. In turn, this shows site-specific expansive strain up to 0.63% in the doped structure throughout the crystal.

A more precise mapping of the localized strain sites can be done by isolating the diffraction intensity specifically associated with the observed local lattice expansion in the Mn-doped 2D perovskite crystals. This was achieved by first splitting the 2θ diffraction spectrum into two regions of interest (ROI) above and below 27.14° . The ROI above relates to the intrinsic structure of Cs₂PbI₂Cl₂, and the ROI below is related to the Mn²⁺ induced local structural expansion (referred to as the Mn-peak). Next, the integrated diffraction intensity of the ROI coinciding with the expansion was mapped across the same spatial region as shown in Figure 3d for both the undoped and doped samples (Figure 4b). The undoped systems showed no diffraction intensity pattern related to the Mn-peak. This is consistent and expected since there was no observation of localized nanoscale strains like the one observed in the Mn-doped samples (Figure 4a). However, in the doped samples, high intensity sites (lime green to red regions) interspersed across the doped sample were observed (Figure 4b). Three such spots are denoted with Roman numerals III, IV, and V, which correspond to varying degrees of Mn-peak intensity. These sites occur at the same regions as the 3.17 Å (0.63% strain) regions in the d-spacing map from Figure 4a. For a better understanding of the diffraction patterns, the average spectrum of a 5 x 5-pixel area for five spots are shown in Figure 4d. Spots I and II are regions across both Cs₂PbI₂Cl₂ and Mn:Cs₂PbI₂Cl₂ 2D perovskites that relate to the intrinsic structure (no nanoscale strain or minimal Mn-peak intensity),

respectively. They show very similar diffraction curves that denote a correlated structure, as expected. In comparison, spot III, IV, and V regions show localized nanoscale strain and medium to high intensity for the Mn-peak. The diffraction curves for spots III and IV relate to regions where signatures from the intrinsic structure and varied degrees of nanoscale strain (Mn-peak) are observed, resulting in multiple peaks. Spot V shows only the Mn-peak while the non-doped perovskite structure peak has vanished. ROI for high 2θ diffraction spectrum maps and further diffraction spectra are presented in the *Supporting Information* Figure S4. These results support the occurrence of spatially distributed defect regions that result in localized expansive strain. Moreover, the occurrence of larger higher intensity regions supports clustering of Mn^{2+} interstitials in the system, which corroborate the results seen by MFM measurements.

Elemental signatures in our samples were investigated through the nanoXRF arm of the scanning X-ray microscopy technique, as described previously. Integrated fluorescence intensity for iodine, cesium, and lead were mapped at each step across both undoped and doped samples

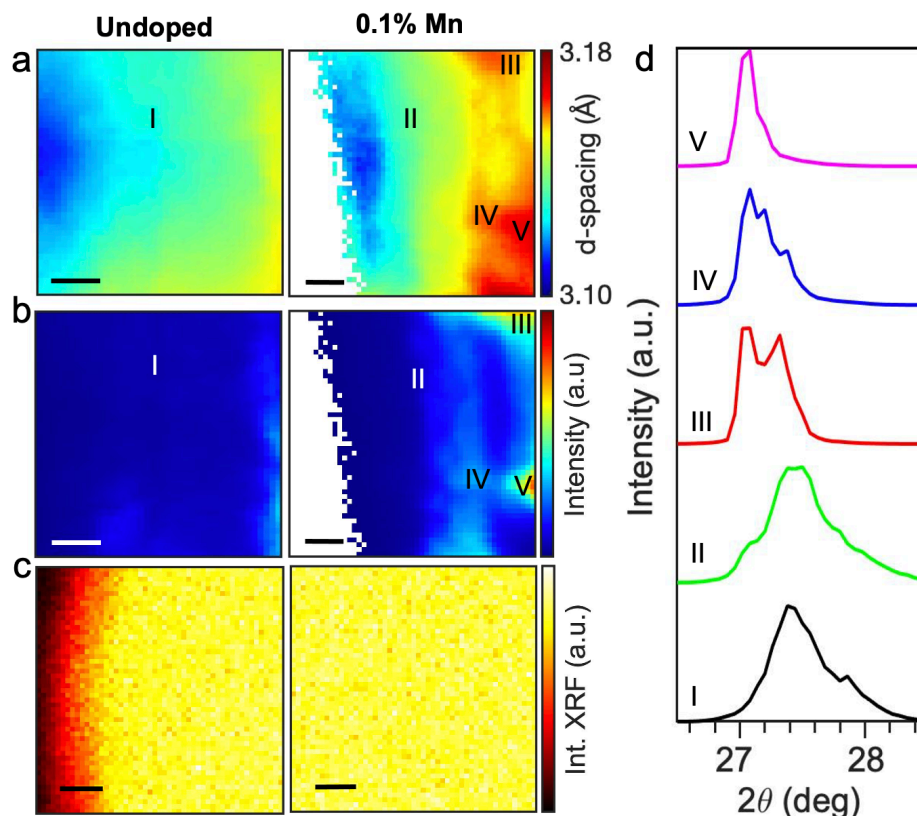


Figure 4. Nanoscale X-Ray Microscopy Mapping. For a-c, undoped (left) vs 0.1% Mn^{2+} (right) (a) d-spacing (b) nanoXRD intensity for ROI below 27.14° (c) nanoXRF of iodine. Scalebar is 150 nm. (d) nanoXRD spectra for (006) peak for the 5×5 -pixel region corresponding the Roman numerals on a & b graphs.

(Figure 4c and Figure S5). $\text{Cs}_2\text{PbI}_2\text{Cl}_2$ and $\text{Mn}:\text{Cs}_2\text{PbI}_2\text{Cl}_2$ samples showed homogenous and consistent fluorescence intensity across the bulk region. In other words, we did not observe anomalies of low fluorescing intensities that corresponded to the nanoXRD local strain mapping results (Figure 4a,b). Due to the extremely dilute amount of manganese incorporated into the sample, the fluorescence signal was at the edge of the instrument capabilities. However, these results imply that perovskite intrinsic lead, iodine, or cesium vacancies are not causing the localized nanoscale strain phenomenon measured by nanoXRD for the Mn-doped sample. The homogeneity of lead, iodine, and cesium further suggests there was no ion migration induced degradation, or phase segregation is negligible. Moreover, the defect that causes these structural strains does not affect the intrinsic 2D perovskite chemical make-up.

The experimental results obtained suggest that Mn-doping in $\text{Cs}_2\text{PbI}_2\text{Cl}_2$ 2D perovskite occurs *via* interstitial incorporation of Mn^{2+} atoms into the lattice. Bulk powder XRD indicate an inhomogeneous dopant incorporation through peak broadening. PL, time-resolved PL, and MFM confirm the incorporation of impurities in the sample that match the optical and magnetic characteristics of Mn^{2+} . Further, 2D MFM mapping show spatially specific regions of these Mn^{2+} signatures. NanoXRD further showed site-specific nanoscale strains occurring throughout $\text{Mn}:\text{Cs}_2\text{PbI}_2\text{Cl}_2$ to be at the origin of the average expansion in the lattice and the broadening effect of the diffraction pattern. In comparison, nanoXRF showed consistency in the chemical make-up of the Mn-doped sample implying that the Mn^{2+} dopants do not substitute lead. To further understand which dopant configuration leads to a local lattice expansion, we performed DFT calculations as described below.

We first calculated changes in the lattice constants of the 2D $\text{Cs}_2\text{PbI}_2\text{Cl}_2$ perovskite upon Mn^{2+} substitutional and interstitial doping (see Methods Section). Optimized lattice constants of one orthorhombic primitive unit cell (previously shown to be stable by DFT calculations)⁶⁹ of 5.74 Å, 5.74 Å, and 19.33 Å for the pristine $\text{Cs}_2\text{PbI}_2\text{Cl}_2$ primitive cell, agree with the measured values of 5.64 Å, 5.64 Å, and 18.88 Å, respectively, within 2.3%. To examine Mn^{2+} doping concentration effects with two doping densities, we chose $3\times3\times1$ and $4\times4\times1$ $\text{Cs}_2\text{PbI}_2\text{Cl}_2$ supercells, corresponding to doping densities of 0.79% and 0.44%. Larger supercells that would mimic the 0.1% experimental doping were too sizable computationally. As an example, we show sections of an optimized $4\times4\times1$ supercell for both substitutionally and interstitially Mn-doped $\text{Cs}_2\text{PbI}_2\text{Cl}_2$ (Figure 5a,d).

The $4 \times 4 \times 1$ supercell of pristine $\text{Cs}_2\text{PbI}_2\text{Cl}_2$ can be found in the *Supporting Information* Figure S6. In the substitutionally doped perovskite, the Mn^{2+} centered octahedra shrink, as compared to the Pb^{2+} centered octahedron. In the interstitially doped perovskite, the Mn^{2+} atom resides between two octahedra, namely in the triangle shown by connecting one Cl^- and two I^- atoms, causing an expansion of the lattice. The trend in the 2D perovskite's structural response is captured irrespective of the exact concentration considered (Table S3), supporting our experimental diffraction results. To understand possible propensity towards clustering of Mn^{2+} atoms, we also examined doping by two Mn^{2+} atoms in the $4 \times 4 \times 1$ supercell. The results indicate that upon substitutional doping, each Mn^{2+} is covered by an I-Cl octahedral shell and separate from the next Mn^{2+} ; thus, not showing a clustering propensity. Upon interstitial doping, however, Mn^{2+} atoms tend to cluster. The structural optimization indicates that the energetically favorable structure occurs when two Mn^{2+} atoms reside in the spaces around the same octahedron with a distance of 2.56 Å between them, as shown in Figure S7. This configuration results in the energy being 1 eV lower than the structure that has two interstitial Mn^{2+} atoms separated by 11.51 Å. We note that two interstitially doped Mn^{2+} atoms in a $4 \times 4 \times 1$ supercell causes a lattice expansion of 0.49% and 0.43% along a_x and a_y , respectively, and 0.08% along a_z . The predicted Mn^{2+} clustering in interstitial doping agrees with the spatial site-specificity of the MFM and nanoXRD results and

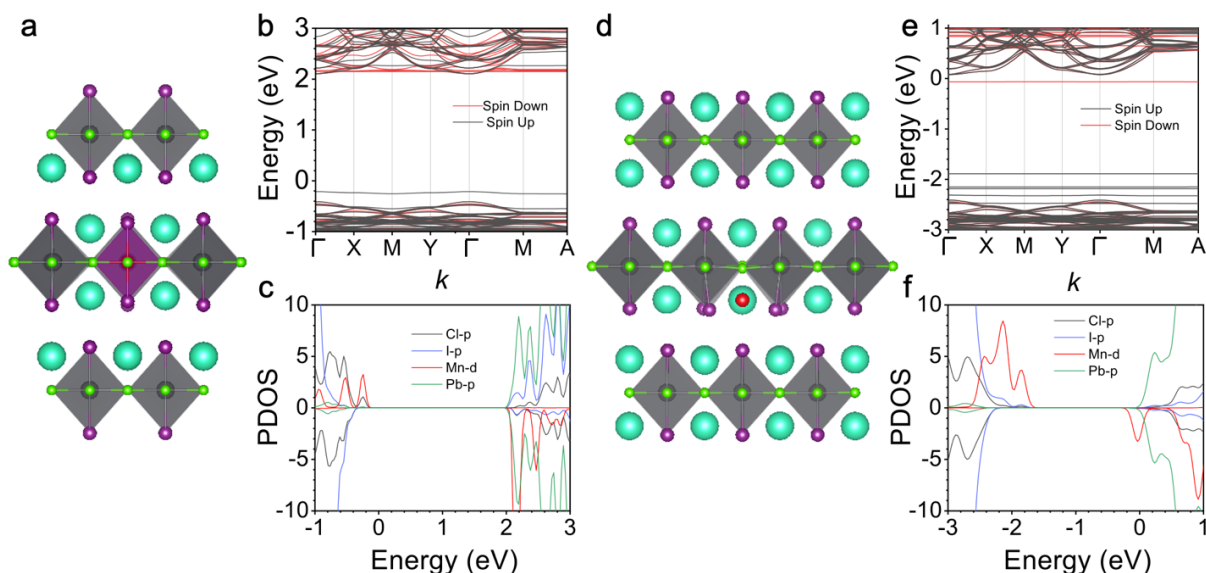


Figure 5. Computational Modeling using DFT. Single Mn^{2+} substitutionally doped 2D $\text{Cs}_2\text{PbI}_2\text{Cl}_2$ (a) crystal structure, with $4 \times 4 \times 1$ supercell (b) band structure and (c) PDOS. Single Mn^{2+} interstitially doped 2D $\text{Cs}_2\text{PbI}_2\text{Cl}_2$ (d) crystal structure, with $4 \times 4 \times 1$ supercell (e) band structure and (f) PDOS. Colors denote Pb-black, Cs-mint green, I-purple, Cl-green, Mn-red. In PDOS panels, positive and negative are for spin up and spin down.

could further explain why a dip in the EPR signal was observed initially.

Next, we summarized the band structures in comparison to the measured PL spectra, also measured previously in other work.⁷⁰ The pristine $\text{Cs}_2\text{PbI}_2\text{Cl}_2$ band structure and PDOS summary can be found in *Supporting Information* Figure S6. As expected, the pristine perovskite conduction band bottom is contributed by Pb p-orbitals, and the valence band top by I and Cl p-orbitals. The band-gap occurs at the Γ k -point of the supercell reciprocal Brillouin zone. The calculated electronic band-gap is 2.50 eV, which is larger than the pure iodide 2D (Cs_2PbI_4) at the same level of theory. This computed band-gap is in reasonable agreement with our measured optical absorption onset and PL emission around 2.88 eV (430 nm) in Figure 2a. There was also agreement with previously measured values of 3.04 eV and 3.01 eV (absorption onset and PL),⁶⁹ as well as ca. 3 eV.⁷⁰ However, this only results from simultaneous neglect of spin-orbit coupling (SOC) effect and many-body corrections, which are both due to limitations of available computational resources for such large systems. Further, we note that because of the need to compare the results to the Mn-doped structures at low concentration, the band structures were calculated using the PBE exchange-correlation functional rather than HSE (Heyd–Scuseria–Ernzerhof),⁷¹ which may cause an underestimation of the band gaps. Therefore, we stress that the following analysis be taken qualitatively, rather than considering the relative changes.

The band structure and PDOS for the substitutionally doped system is summarized in Figure 5b,c, while the interstitially doped system is shown in Figure 5e,f. The band gaps between dispersive bands only slightly change from 2.50 eV to 2.51 eV and 2.49 eV for substitutional and interstitial doping at 0.44% concentration, respectively. Upon either Mn^{2+} doping mode, middle gap states introduced by the impurity appear. For substitutional doping, there is one spin up middle gap band at 0.2 eV above the valence band top. The PDOS indicate that the band is contributed by Mn^{2+} d-orbitals and its bonded Cl p-orbitals. For interstitial doping, there is one spin down middle gap band at 0.17 eV below the conduction band bottom, and there are four spin up middle gap bands up to 0.60 eV above the valence band top. Therefore, in addition to the PL emission at the band gap, we expect another emission band red-shifted in energy by about 0.2 eV for substitutional doping and 0.8 eV for interstitial doping. Our Mn^{2+} induced PL emission occurs at 2.07 eV (599 nm), as shown in Figure 2a, and is 0.81 eV red-shifted from the emission at 2.88 eV (430 nm). Here, the interstitial model predicted a similar relative change as observed in our PL measurement for the doped perovskite. At this level of theory, it could conceivably be suggested the red-shifted

emission for interstitial doping may be assigned to the Mn d-d transition from the spin up Mn d-state residing 0.6 eV above the VB to the spin down Mn d-state residing 0.17 eV below the CB (Figure 5f). Moreover, the transition from a spin up to spin down state potentially also contributing to the long lifetime of the emission. We want to emphasize again that rigorous many-body band structures and optical gap calculations, such as using the GW (Green's function approximation with a screened Coulomb interaction W) and GW-BSE (Bethe Salpeter Equation) levels of theory, including SOC, are beyond the scope of this study. Our computational results demonstrate that interstitial incorporation, not substitutional, of Mn^{2+} in the 2D $\text{Cs}_2\text{PbI}_2\text{Cl}_2$ perovskite supports the observed lattice expansion and, at this level of theory, can account for the appearance of a PL emission peak at 2.07 eV (599 nm).

Conclusion

Our work provides insight into the dopant-host interactions, nanoscale structure, and chemical composition in 2D halide perovskites by using a multiscale experiment-modeling approach. In contradiction to previous reports, we show that the Mn^{2+} dopants are incorporated into the perovskite lattice *via* interstitial doping, instead of divalent substitution. This led to yellowish-orange emission and expansions in the lattice causing localized nanoscale strains. The presence of conglomerating Mn^{2+} interstitials will need to be addressed in future work if atomic defects are desired. Further, this may negatively affect wanted magnetic and electronic functionalities. As learned from III-V semiconductors, synthesis strategies that influence incorporation mode include chemical vapor deposition or post-growth annealing. The deeper understanding of the local placement and structural changes from metal dopants in the 2D HaP will help further their potential in optoelectronic and spintronic applications, such as in photovoltaics, high temperature ferromagnetic semiconductors, or spin-polarized single photon emission for quantum information technologies of the future.

Methods

Sample Preparation: CsI (Sigma Aldrich, 99.999%), PbCl_2 (Sigma Aldrich, 99.999%), and MnCl_2 (Sigma Aldrich, >99%) were used as received. For the preparation of 1%-doped sample, 1.000 g of CsI was mixed and thoroughly ground with 0.5298 g of PbCl_2 and 0.0024 g of MnCl_2 . The samples with 5 and 10% nominal doping were prepared by using 0.5084 and 0.4817 g of PbCl_2 along with 0.0121 and 0.0242 g of MnCl_2 , respectively. Because of the small amount of MnCl_2 used in the preparation of 0.1%-doped sample, MnCl_2 was added on top of the stoichiometric amounts of CsI and PbCl_2 , which were taken in a 2:1 molar ratio. The ground reagents were loaded

into a 7 mm ID silica tube and sealed under dynamic vacuum. All three reactions were placed in a tube furnace and heated to 500 °C in 10 hours, dwelled at this temperature for 12 h and slowly cooled to room temperature over 3 days. The product contained transparent crystal ingots along with unknown impurities on the walls of the tube and the ingots. The impurities were removed mechanically using a sharp blade and the crystal ingots were cleaved for further characterization.

Powder X-Ray Diffraction: PXRD patterns were collected on ground single crystals of all samples. A Rigaku Miniflex600 equipped with a Dtex silicon 1D detector was used to obtain powder X-ray diffraction patterns. Cu K α radiation ($\lambda = 1.5406$ Å) was produced using 40 kV and 15 mA and filtered with a graphite monochromator and K β foil filter. A zero-background silicon holder was used. Analysis of the peaks and lattice parameters were carried out through Rietveld refinements using the program Profex, a BGMN version 4.2.23 based program.

Electron Paramagnetic Resonance: EPR measurements were performed at X-band (~9.68 GHz) using a Bruker Elexsys E580-X EPR spectrometer outfitted with a Bruker ER-4122SHQE resonator. The continuous-wave EPR spectra were collected at room temperature, using non-saturating microwave power (~4 mW) and 0.2 mT field modulation at 100 kHz.

Scanning X-ray Microscopy: SXM was conducted through the Center for Nanoscale Materials at the Advanced Proton Source at Argonne National Laboratory and used to collect diffraction and fluorescence signals. Samples were exfoliated micro-crystals on a silicon-based substrate. The SXM set up was equipped with a Fresnel zone plate (Xradia Inc.) that focuses a monochromatic X-ray beam of 1.4857 Å (8.345 keV) producing a photon flux of 3×10^8 photons/second. The X-ray scanned across a ROI at 20 nm steps to give a 2D map of diffraction patterns and fluorescence intensities. For diffraction, the reflected signal was collected on a pixel-array detector (Medipix) of 2θ range 20°-50° and positioned for the out-of-plane 006 Bragg condition to obtain diffraction patterns.⁷² Further, the pattern was integrated for intensity and centroidal 2θ calculated, where Bragg's Law was employed to obtain d-spacing. For fluorescence, the system is equipped with a single-element detector (low resolution) for locating the sample, and a four-element detector (high resolution) for precise measurements. The fluorescence signal was collected and integrated for specific energy regions related to the element of interest to obtain intensity.

Chromium markers were deposited on the substrate prior to exfoliation of the crystals for positioning. From there, iodine was utilized to pinpoint the micrometer sized single crystals and ROIs as it had the largest fluorescing yield compared to the elements in the host HaP, Cs₂PbI₂Cl₂, or Mn dopant (order highest to lowest yield: iodine, cesium, lead, and manganese)⁷³. The undoped sample was exfoliated on a special substrate called a 'diving board' that allowed the incident X-ray beam to transmit through to the four-element fluorescence detector. This gave diffraction and fluorescence signals concurrently. The 0.1% Mn doped sample used a thicker Si-substrate, which the beam could not transmit. Here, the sample was rotated 120° and the reflected signal recorded by the four-element fluorescence detector.

Magnetic Force Microscopy: Magnetic force microscopy (MFM) was conducted on an MFP-3D Origin AFM (Asylum Research, Oxford Instruments, CA) with a dual-pass technique using Co/Cr coated AFM probes (MSEP-V2), where a conventional tapping mode was performed in the first pass and the MFM was followed in the second pass (Nap Mode). Prior to the experiment, the AFM probe was magnetized by a strong Neodymium rare-earth magnet. The 2D inorganic halide

perovskite (HaP) samples were mechanically exfoliated onto a clean silicon wafer by the classical scotch tape method. Thin flakes of HaP were first identified by optical microscope for MFM characterization. During MFM measurement, the AFM tip was lifted off from the sample surface and maintained a constant separation about (~ 15 nm). The AFM probe was driven to oscillate at its resonant frequency by the shake piezo on the AFM cantilever holder. The magnetic force between the AFM probe and the sample surface induces phase shifts during the Nap Mode, which provides the contrast of magnetic response of the sample surfaces. Repulsive and attractive magnetic forces increase (bright contrast) and decrease (dark contrast) the phase shift, respectively.

Photoluminescence Spectroscopy: Photoluminescence (PL) spectra for initial characterization on the Mn-doped samples in Figure 1c were acquired using 405 nm LEDs for excitation and an OceanOptics USB4000 spectrometer.

A FLS1000 fluorimeter from Edinburgh Instruments (Livingston, Scotland) was employed for steady-state and time-resolved PL measurements in Figures 3a,b. Excitation at 314 nm was generated using either a 450 W Xe arc lamp connected to a double grating Czerny-Turner monochromator for steady-state PL measurements or a 100 W Xe microsecond pulsed flash lamp (model μ F2) connected to a double grating Czerny-Turner monochromator for time-resolved PL measurements. The emission signal is collected at 90° relative to the excitation source and passed through a Czerny-Turner monochromator prior to being collected with a Hamamatsu R928P side window photomultiplier in a cooled housing (Operating temperature: -22°C). For steady-state measurements, an excitation bandwidth of 1.50 nm and emission bandwidth of 15 nm were used. Data was collected from 350 nm – 800 nm with a step-size of 1 nm and a dwell time of 0.200 s. For time-resolved measurements, the flash lamp was operated at a pulse frequency of 100 Hz. An excitation bandwidth of 0.60 nm was used. The PL signal was monitored at 590 nm with a slit width of 18 nm. Appropriate filters were used to block stray light from the excitation source for all PL measurements.

Computational Modeling: DFT calculations were carried out with the Vienna *ab initio* simulation package VASP 5.4.^{74,75} The Kohn-Sham equations are solved using a plane wave basis set with an energy cutoff of 550 eV, and the projector augmented-wave (PAW) potential was applied.⁷⁵ A $2\times 2\times 2$ k-point sampling was used for the $3\times 3\times 1$ supercell, and $1\times 1\times 2$ for the $4\times 4\times 1$ supercell. The crystal structure was optimized using the PBE (Perdew-Burke-Ernzerhof) exchange-correlation functional⁷⁶ with spin-polarization. We also applied the zero damping D3 correction of Grimme,⁷⁷ as inclusion of London dispersion in the functional for treating halide perovskites was emphasized,⁷⁸ and previously applied. Geometries were fully relaxed regarding lattice parameters and interatomic distances until forces were less than 0.01 eV/Å.

Acknowledgments

The work at Rice University was supported by the DoD-STIR program funded by ARO. W.L acknowledges NSF GRFP. The material is based upon work supported by the National Science Foundation Graduate Research Fellowship Program under Grant No. (NSF 20-587). Any opinions, findings, and conclusions expressed in this material are those of the author and do not necessarily reflect the views of the National Science Foundation. M.V.H. acknowledges use of the Center for Nanoscale Materials and Advanced Photon Source, both Office of Science user

facilities, was supported by the U.S. Department of Energy, Office of Science, Office of Basic Energy Sciences, under Contract No. DE-AC02-06CH11357. J.E. and C.K. acknowledges the financial support from the Institut Universitaire de France. At Northwestern, the work was primarily supported by the Department of Energy, Office of Science, Basic Energy Sciences, under Grant No. SC0012541 (sample synthesis and structure and property characterization) and under Award DE-FG02-99ER14999 (EPR characterization). Q.T. acknowledges support through the startup funds from the Texas A&M Engineering Experiment Station (TEES) and the Texas A&M Triads for Transformation (T3) grant (MFM characterization). All AFRL affiliated authors recognize funding support from the Air Force Research Laboratory/RXAP contract FA8650-16-D-5402-0001 (photo-response characterization) and the helpful support and computer resources from the DoD High-Performance Computing Modernization Program (DFT calculations). This research was performed while M.C.B. held an NRC Research Associateship award at the Air Force Research Laboratory.

Supporting Information:

Supporting Information is available free of charge online.

- Synthesis schematic, optical and fluorescence under UV images of bulk crystals, table of PXRD Rietveld refinements, TRPL fitting parameters of 2.07 eV emission, AFM height images, examples of CCD images from nanoXRD, nanoXRD 2D mapping for high diffraction angle ROI, nanoXRF 2D mapping for lead and cesium, DFT calculated lattice constants for Mn-doped structures, pristine 4x4x1 supercell structure with corresponding band structure and PDOS, and double interstitially Mn-doped supercell structure.

References:

- (1) Hu, H.; Zhang, W. Synthesis and Properties of Transition Metals and Rare-Earth Metals Doped ZnS Nanoparticles. *Opt. Mater.* **2006**, *28*, 536–550.
- (2) Gaj, J. A.; Kossut, J. *Introduction to the Physics of Diluted Magnetic Semiconductors*; Kossut, J., Gaj, J. A., Eds.; Springer Series in Materials Science; Springer Verlag: Berlin, Heidelberg, 2010.
- (3) Pradhan, N. Mn-Doped Semiconductor Nanocrystals: 25 Years and Beyond. *J. Phys. Chem. Lett.* **2019**, *10*, 2574–2577.
- (4) Ohno, H. Making Nonmagnetic Semiconductors Ferromagnetic. *Science* **1998**, *281*, 951–956.
- (5) Karan, N. S.; Sarma, D. D.; Kadam, R. M.; Pradhan, N. Doping Transition Metal (Mn or Cu) Ions in Semiconductor Nanocrystals. *J. Phys. Chem. Lett.* **2010**, *1*, 2863–2866.
- (6) Bhargava, R. N.; Gallagher, D.; Hong, X.; Nurmikko, A. Optical Properties of Manganese-Doped Nanocrystals of ZnS. *Phys. Rev. Lett.* **1994**, *72*, 416–419.
- (7) Norris, D. J.; Yao, N.; Charnock, F. T.; Kennedy, T. A. High-Quality Manganese-Doped ZnSe Nanocrystals. *Nano Lett.* **2001**, *1*, 3–7.
- (8) Pradhan, N.; Goorskey, D.; Thessing, J.; Peng, X. An Alternative of CdSe Nanocrystal Emitters: Pure and Tunable Impurity Emissions in ZnSe Nanocrystals. *J. Am. Chem. Soc.* **2005**, *127*, 17586–17587.

- (9) Yang, Y.; Chen, O.; Angerhofer, A.; Cao, Y. C. Radial-Position-Controlled Doping in CdS/ZnS Core/Shell Nanocrystals. *J. Am. Chem. Soc.* **2006**, *128*, 12428–12429.
- (10) Acharya, S.; Sarma, D. D.; Jana, N. R.; Pradhan, N. An Alternate Route to High-Quality ZnSe and Mn-Doped ZnSe Nanocrystals. *J. Phys. Chem. Lett.* **2010**, *1*, 485–488.
- (11) Mikulec, F. V.; Kuno, M.; Bennati, M.; Hall, D. A.; Griffin, R. G.; Bawendi, M. G. Organometallic Synthesis and Spectroscopic Characterization of Manganese-Doped CdSe Nanocrystals. *J. Am. Chem. Soc.* **2000**, *122*, 2532–2540.
- (12) Vlaskin, V. A.; Janssen, N.; van Rijssel, J.; Beaulac, R.; Gamelin, D. R. Tunable Dual Emission in Doped Semiconductor Nanocrystals. *Nano Lett.* **2010**, *10*, 3670–3674.
- (13) Beaulac, R.; Archer, P. I.; van Rijssel, J.; Meijerink, A.; Gamelin, D. R. Exciton Storage by Mn²⁺ in Colloidal Mn²⁺-Doped CdSe Quantum Dots. *Nano Lett.* **2008**, *8*, 2949–2953.
- (14) Borschel, C.; Messing, M. E.; Borgström, M. T.; Paschoal, W.; Wallentin, J.; Kumar, S.; Mergenthaler, K.; Deppert, K.; Canali, C. M.; Pettersson, H.; Samuelson, L.; Ronning, C. A New Route toward Semiconductor Nanospintronics: Highly Mn-Doped GaAs Nanowires Realized by Ion-Implantation under Dynamic Annealing Conditions. *Nano Lett.* **2011**, *11*, 3935–3940.
- (15) Edmonds, K. W.; Bogusławski, P.; Wang, K. Y.; Champion, R. P.; Novikov, S. N.; Farley, N. R. S.; Gallagher, B. L.; Foxon, C. T.; Sawicki, M.; Dietl, T.; Buongiorno Nardelli, M.; Bernholc, J. Mn Interstitial Diffusion in (Ga,Mn)As. *Phys. Rev. Lett.* **2004**, *92*, 037201.
- (16) Raebiger, H.; Ganchenkova, M.; von Boehm, J. Diffusion and Clustering of Substitutional Mn in (Ga,Mn)As. *Appl. Phys. Lett.* **2006**, *89*, 012505.
- (17) Prucnal, S.; Gao, K.; Skorupa, I.; Rebohle, L.; Vines, L.; Schmidt, H.; Khalid, M.; Wang, Y.; Weschke, E.; Skorupa, W.; Grenzer, J.; Hübner, R.; Helm, M.; Zhou, S. Band-Gap Narrowing in Mn-Doped GaAs Probed by Room-Temperature Photoluminescence. *Phys. Rev. B* **2015**, *92*, 224407.
- (18) Zhang, Y.; Xie, Z.-X.; Deng, Y.-X.; Yu, X. Impurity Distribution and Ferromagnetism in Mn-Doped GaAs Nanowires: A First-Principle Study. *Phys. Lett. A* **2015**, *379*, 2745–2749.
- (19) Santra, P. K.; Kamat, P. V. Mn-Doped Quantum Dot Sensitized Solar Cells: A Strategy to Boost Efficiency over 5%. *J. Am. Chem. Soc.* **2012**, *134*, 2508–2511.
- (20) Dong, Y.; Choi, J.; Jeong, H.-K.; Son, D. H. Hot Electrons Generated from Doped Quantum Dots via Upconversion of Excitons to Hot Charge Carriers for Enhanced Photocatalysis. *J. Am. Chem. Soc.* **2015**, *137*, 5549–5554.
- (21) Ohya, S.; Ohno, K.; Tanaka, M. Magneto-Optical and Magnetotransport Properties of Heavily Mn-Doped GaMnAs. *Appl. Phys. Lett.* **2007**, *90*, 112503.
- (22) Jadhav, P. A.; Panmand, R. P.; Patil, D. R.; Fouad, H.; Gosavi, S. W.; Kale, B. B. Triangular CdS Nanostructure: Effect of Mn Doping on Photoluminescence, Electron Spin Resonance, and Magneto-Optical Properties. *J. Nanoparticle Res.* **2017**, *19*, 218.
- (23) Krstajić, P.; Peeters, F.; Ivanov, V.; Fleurov, V.; Kikoin, K. Double-Exchange Mechanisms for Mn-Doped III-V Ferromagnetic Semiconductors. *Phys. Rev. B* **2004**, *70*, 195215.
- (24) Stroppa, A.; Picozzi, S.; Continenza, A.; Freeman, A. J. Electronic Structure and Ferromagnetism of Mn-Doped Group-IV Semiconductors. *Phys. Rev. B* **2003**, *68*, 155203.
- (25) Sharma, P.; Gupta, A.; Rao, K. V.; Owens, F. J.; Sharma, R.; Ahuja, R.; Guillen, J. M. O.; Johansson, B.; Gehring, G. A. Ferromagnetism above Room Temperature in Bulk and Transparent Thin Films of Mn-Doped ZnO. *Nat. Mater.* **2003**, *2*, 673–677.

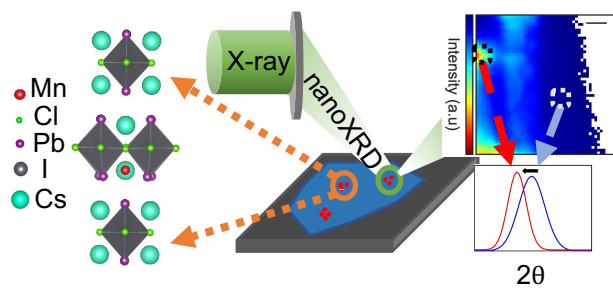
- (26) Nazmul, A. M.; Amemiya, T.; Shuto, Y.; Sugahara, S.; Tanaka, M. High Temperature Ferromagnetism in GaAs-Based Heterostructures with Mn δ Doping. *Phys. Rev. Lett.* **2005**, *95*, 017201.
- (27) Han, D. S.; Park, J.; Rhie, K. W.; Kim, S.; Chang, J. Ferromagnetic Mn-Doped GaN Nanowires. *Appl. Phys. Lett.* **2005**, *86*, 032506.
- (28) Gould, C.; Schmidt, G.; Richter, G.; Fiederling, R.; Grabs, P.; Molenkamp, L. W. Spin Injection into Semiconductors Using Dilute Magnetic Semiconductors. *Appl. Surf. Sci.* **2002**, *190*, 395–402.
- (29) Hao, S.; Zhou, G.; Wu, J.; Duan, W.; Gu, B.-L. Spin-Polarized Electron Emitter: Mn-Doped GaN Nanotubes and Their Arrays. *Phys. Rev. B* **2004**, *69*, 113403.
- (30) Viswanatha, R.; Pietryga, J. M.; Klimov, V. I.; Crooker, S. A. Spin-Polarized Mn²⁺ Emission from Mn-Doped Colloidal Nanocrystals. *Phys. Rev. Lett.* **2011**, *107*, 067402.
- (31) Ray, O.; Sirenko, A. A.; Berry, J. J.; Samarth, N.; Gupta, J. A.; Malajovich, I.; Awschalom, D. D. Exciton Spin Polarization in Magnetic Semiconductor Quantum Wires. *Appl. Phys. Lett.* **2000**, *76*, 1167–1169.
- (32) Xue, J.; Wang, R.; Yang, Y. The Surface of Halide Perovskites from Nano to Bulk. *Nat. Rev. Mater.* **2020**, *5*, 809–827.
- (33) Xiao, Z.; Song, Z.; Yan, Y. From Lead Halide Perovskites to Lead-Free Metal Halide Perovskites and Perovskite Derivatives. *Adv. Mater.* **2019**, *31*, 1803792.
- (34) Blancon, J.-C.; Even, J.; Stoumpos, Costas. C.; Kanatzidis, Mercouri. G.; Mohite, A. D. Semiconductor Physics of Organic–Inorganic 2D Halide Perovskites. *Nat. Nanotechnol.* **2020**, *15*, 969–985.
- (35) Saparov, B.; Mitzi, D. B. Organic–Inorganic Perovskites: Structural Versatility for Functional Materials Design. *Chem. Rev.* **2016**, *116*, 4558–4596.
- (36) Mao, L.; Stoumpos, C. C.; Kanatzidis, M. G. Two-Dimensional Hybrid Halide Perovskites: Principles and Promises. *J. Am. Chem. Soc.* **2019**, *141*, 1171–1190.
- (37) Blancon, J.-C.; Stier, A. V.; Tsai, H.; Nie, W.; Stoumpos, C. C.; Traoré, B.; Pedesseau, L.; Kepenekian, M.; Katsutani, F.; Noe, G. T.; Kono, J.; Tretiak, S.; Crooker, S. A.; Katan, C.; Kanatzidis, M. G.; Crochet, J. J.; Even, J.; Mohite, A. D. Scaling Law for Excitons in 2D Perovskite Quantum Wells. *Nat. Commun.* **2018**, *9*, 2254.
- (38) Gong, X.; Voznyy, O.; Jain, A.; Liu, W.; Sabatini, R.; Piontkowski, Z.; Walters, G.; Bappi, G.; Nokhrin, S.; Bushuyev, O.; Yuan, M.; Comin, R.; McCamant, D.; Kelley, S. O.; Sargent, E. H. Electron–Phonon Interaction in Efficient Perovskite Blue Emitters. *Nat. Mater.* **2018**, *17*, 550–556.
- (39) Leng, K.; Fu, W.; Liu, Y.; Chhowalla, M.; Loh, K. P. From Bulk to Molecularly Thin Hybrid Perovskites. *Nat. Rev. Mater.* **2020**, *5*, 482–500.
- (40) Liu, H.; Wu, Z.; Shao, J.; Yao, D.; Gao, H.; Liu, Y.; Yu, W.; Zhang, H.; Yang, B. CsPb_xMn_{1-x}Cl₃ Perovskite Quantum Dots with High Mn Substitution Ratio. *ACS Nano* **2017**, *11*, 2239–2247.
- (41) Liu, W.; Zheng, J.; Shang, M.; Fang, Z.; Chou, K.-C.; Yang, W.; Hou, X.; Wu, T. Electron-Beam Irradiation-Hard Metal-Halide Perovskite Nanocrystals. *J. Mater. Chem. A* **2019**, *7*, 10912–10917.
- (42) Mir, W. J.; Jagadeeswararao, M.; Das, S.; Nag, A. Colloidal Mn-Doped Cesium Lead Halide Perovskite Nanoplatelets. *ACS Energy Lett.* **2017**, *2*, 537–543.

- (43) Das Adhikari, S.; Guria, A. K.; Pradhan, N. Insights of Doping and the Photoluminescence Properties of Mn-Doped Perovskite Nanocrystals. *J. Phys. Chem. Lett.* **2019**, *10*, 2250–2257.
- (44) Rossi, D.; Parobek, D.; Dong, Y.; Son, D. H. Dynamics of Exciton–Mn Energy Transfer in Mn-Doped CsPbCl₃ Perovskite Nanocrystals. *J. Phys. Chem. C* **2017**, *121*, 17143–17149.
- (45) Xu, K.; Lin, C. C.; Xie, X.; Meijerink, A. Efficient and Stable Luminescence from Mn²⁺ in Core and Core–Isocrystalline Shell CsPbCl₃ Perovskite Nanocrystals. *Chem. Mater.* **2017**, *29*, 4265–4272.
- (46) Zhang, X.; Li, L.; Sun, Z.; Luo, J. Rational Chemical Doping of Metal Halide Perovskites. *Chem. Soc. Rev.* **2019**, *48*, 517–539.
- (47) Sheikh, T.; Nag, A. Mn Doping in Centimeter-Sized Layered 2D Butylammonium Lead Bromide (BA₂PbBr₄) Single Crystals and Their Optical Properties. *J. Phys. Chem. C* **2019**, *123*, 9420–9427.
- (48) Zhou, G.; Jia, X.; Guo, S.; Molokeev, M.; Zhang, J.; Xia, Z. Role of Halogen Atoms on High-Efficiency Mn²⁺ Emission in Two-Dimensional Hybrid Perovskites. *J. Phys. Chem. Lett.* **2019**, *10*, 4706–4712.
- (49) Guria, A. K.; Dutta, S. K.; Adhikari, S. D.; Pradhan, N. Doping Mn²⁺ in Lead Halide Perovskite Nanocrystals: Successes and Challenges. *ACS Energy Lett.* **2017**, *2*, 1014–1021.
- (50) Sun, Q.; Wang, S.; Zhao, C.; Leng, J.; Tian, W.; Jin, S. Excitation-Dependent Emission Color Tuning from an Individual Mn-Doped Perovskite Microcrystal. *J. Am. Chem. Soc.* **2019**, *141*, 20089–20096.
- (51) Dutta, S. K.; Dutta, A.; Das Adhikari, S.; Pradhan, N. Doping Mn²⁺ in Single-Crystalline Layered Perovskite Microcrystals. *ACS Energy Lett.* **2019**, *4*, 343–351.
- (52) Liu, W.; Lin, Q.; Li, H.; Wu, K.; Robel, I.; Pietryga, J. M.; Klimov, V. I. Mn²⁺-Doped Lead Halide Perovskite Nanocrystals with Dual-Color Emission Controlled by Halide Content. *J. Am. Chem. Soc.* **2016**, *138*, 14954–14961.
- (53) Sun, C.; Gao, Z.; Deng, Y.; Liu, H.; Wang, L.; Su, S.; Li, P.; Li, H.; Zhang, Z.; Bi, W. Orange to Red, Emission-Tunable Mn-Doped Two-Dimensional Perovskites with High Luminescence and Stability. *ACS Appl. Mater. Interfaces* **2019**, *11*, 34109–34116.
- (54) De Siena, M. C.; Sommer, D. E.; Creutz, S. E.; Dunham, S. T.; Gamelin, D. R. Spinodal Decomposition during Anion Exchange in Colloidal Mn²⁺-Doped CsPbX₃ (X = Cl, Br) Perovskite Nanocrystals. *Chem. Mater.* **2019**, *31*, 7711–7722.
- (55) Krebs, J. J. EPR Determination of the Nearest-Neighbor Exchange Constant for Mn²⁺ Pairs in KZnF₃. *J. Appl. Phys.* **1969**, *40*, 1137–1139.
- (56) Neumann, T.; Feldmann, S.; Moser, P.; Delhomme, A.; Zerhoch, J.; van de Goor, T.; Wang, S.; Dyksik, M.; Winkler, T.; Finley, J. J.; Plochocka, P.; Brandt, M. S.; Faugeras, C.; Stier, A. V.; Deschler, F. Manganese Doping for Enhanced Magnetic Brightening and Circular Polarization Control of Dark Excitons in Paramagnetic Layered Hybrid Metal-Halide Perovskites. *Nat. Commun.* **2021**, *12*, 3489.
- (57) Shannon, R. D. Revised Effective Ionic Radii and Systematic Studies of Interatomic Distances in Halides and Chalcogenides. *Acta Crystallogr. Sect. A* **1976**, *32*, 751–767.
- (58) Acharyya, P.; Maji, K.; Kundu, K.; Biswas, K. 2D Nanoplates and Scaled-Up Bulk Polycrystals of Ruddlesden–Popper Cs₂PbI₂Cl₂ for Optoelectronic Applications. *ACS Appl. Nano Mater.* **2020**, *3*, 877–886.

- (59) Dutta, A.; Behera, R. K.; Deb, S.; Baitalik, S.; Pradhan, N. Doping Mn(II) in All-Inorganic Ruddlesden–Popper Phase of Tetragonal Cs₂PbCl₂I₂ Perovskite Nanoplatelets. *J. Phys. Chem. Lett.* **2019**, *10*, 1954–1959.
- (60) Das Adhikari, S.; Dutta, S. K.; Dutta, A.; Guria, A. K.; Pradhan, N. Chemically Tailoring the Dopant Emission in Manganese-Doped CsPbCl₃ Perovskite Nanocrystals. *Angew. Chem. Int. Ed.* **2017**, *56*, 8746–8750.
- (61) Usman, M. H. P.; Bakthavatsalam, R.; Kundu, J. Colloidal Mn²⁺ Doped 2D (*n* = 1) Lead Bromide Perovskites: Efficient Energy Transfer and Role of Anion in Doping Mechanism. *ChemistrySelect* **2018**, *3*, 6585–6595.
- (62) Biswas, A.; Bakthavatsalam, R.; Kundu, J. Efficient Exciton to Dopant Energy Transfer in Mn²⁺-Doped (C₄H₉NH₃)₂PbBr₄ Two-Dimensional (2D) Layered Perovskites. *Chem. Mater.* **2017**, *29*, 7816–7825.
- (63) Zhou, G.; Jiang, X.; Molokeev, M.; Lin, Z.; Zhao, J.; Wang, J.; Xia, Z. Optically Modulated Ultra-Broad-Band Warm White Emission in Mn²⁺-Doped (C₆H₁₈N₂O₂)PbBr₄ Hybrid Metal Halide Phosphor. *Chem. Mater.* **2019**, *31*, 5788–5795.
- (64) Su, B.; Molokeev, M. S.; Xia, Z. Unveiling Mn²⁺ Dopant States in Two-Dimensional Halide Perovskite toward Highly Efficient Photoluminescence. *J. Phys. Chem. Lett.* **2020**, *11*, 2510–2517.
- (65) Luo, B.; Guo, Y.; Li, X.; Xiao, Y.; Huang, X.; Zhang, J. Z. Efficient Trap-Mediated Mn²⁺ Dopant Emission in Two Dimensional Single-Layered Perovskite (CH₃CH₂NH₃)₂PbBr₄. *J. Phys. Chem. C* **2019**, *123*, 14239–14245.
- (66) Phung, N.; Félix, R.; Meggiolaro, D.; Al-Ashouri, A.; Sousa e Silva, G.; Hartmann, C.; Hidalgo, J.; Köbler, H.; Mosconi, E.; Lai, B.; Gunder, R.; Li, M.; Wang, K.-L.; Wang, Z.-K.; Nie, K.; Handick, E.; Wilks, R. G.; Marquez, J. A.; Rech, B.; Unold, T.; *et al.* The Doping Mechanism of Halide Perovskite Unveiled by Alkaline Earth Metals. *J. Am. Chem. Soc.* **2020**, *142*, 2364–2374.
- (67) Cortecchia, D.; Mróz, W.; Neutzner, S.; Borzda, T.; Folpini, G.; Brescia, R.; Petrozza, A. Defect Engineering in 2D Perovskite by Mn(II) Doping for Light-Emitting Applications. *Chem* **2019**, *5*, 2146–2158.
- (68) Ren, L.; Wang, Y.; Wang, M.; Wang, S.; Zhao, Y.; Cazorla, C.; Chen, C.; Wu, T.; Jin, K. Tuning Magnetism and Photocurrent in Mn-Doped Organic–Inorganic Perovskites. *J. Phys. Chem. Lett.* **2020**, *11*, 2577–2584.
- (69) Li, J.; Yu, Q.; He, Y.; Stoumpos, C. C.; Niu, G.; Trimarchi, G. G.; Guo, H.; Dong, G.; Wang, D.; Wang, L.; Kanatzidis, M. G. Cs₂PbI₂Cl₂, All-Inorganic Two-Dimensional Ruddlesden–Popper Mixed Halide Perovskite with Optoelectronic Response. *J. Am. Chem. Soc.* **2018**, *140*, 11085–11090.
- (70) Acharyya, P.; Kundu, K.; Biswas, K. 2D Layered All-Inorganic Halide Perovskites: Recent Trends in Their Structure, Synthesis and Properties. *Nanoscale* **2020**, *12*, 21094–21117.
- (71) Heyd, J.; Scuseria, G. E.; Ernzerhof, M. Hybrid Functionals Based on a Screened Coulomb Potential. *J. Chem. Phys.* **2003**, *118*, 8207–8215.
- (72) Holt, M.; Harder, R.; Winarski, R.; Rose, V. Nanoscale Hard X-Ray Microscopy Methods for Materials Studies. *Annu. Rev. Mater. Res.* **2013**, *43*, 183–211.
- (73) Kirz, J.; Attwood, D. T.; Henke, B. L.; Howells, M. R.; Kennedy, K. D.; Kim, K.-J.; Kortright, J. B.; Perera, R. C. C.; Pianetta, P.; Riordan, J. C.; Scofield, J. H.; Stradling, G. L.; Thompson, A. C.; Underwood, J. H.; Williams, G. P.; Winick, H. *Center for X-Ray*

Optics, X-Ray Data Booklet; Vaughan, D., Eds.; Lawrence Berkeley National Laboratory: Berkely, 1986.

- (74) Kresse, G.; Furthmüller, J. Efficiency of *ab Initio* Total Energy Calculations for Metals and Semiconductors Using a Plane-Wave Basis Set. *Comput. Mater. Sci.* **1996**, *6*, 15–50.
- (75) Kresse, G.; Joubert, D. From Ultrasoft Pseudopotentials to the Projector Augmented-Wave Method. *Phys. Rev. B* **1999**, *59*, 1758–1775.
- (76) Perdew, J. P.; Burke, K.; Ernzerhof, M. Generalized Gradient Approximation Made Simple. *Phys. Rev. Lett.* **1996**, *77*, 3865–3868.
- (77) Grimme, S.; Antony, J.; Ehrlich, S.; Krieg, H. A Consistent and Accurate *ab Initio* Parametrization of Density Functional Dispersion Correction (DFT-D) for the 94 Elements H-Pu. *J. Chem. Phys.* **2010**, *132*, 154104.
- (78) Beck, H.; Gehrmann, C.; Egger, D. A. Structure and Binding in Halide Perovskites: Analysis of Static and Dynamic Effects from Dispersion-Corrected Density Functional Theory. *APL Mater.* **2019**, *7*, 021108.
- (79) Zhang, L.; Liang, W. How the Structures and Properties of Two-Dimensional Layered Perovskites MAPbI₃ and CsPbI₃ Vary with the Number of Layers. *J. Phys. Chem. Lett.* **2017**, *8*, 1517–1523.



For Table of Contents Only